UDC 539.3, 548.0 Вестник СПбГУ. Математика. Механика. Астрономия. 2022. Т. 9 (67). Вып. 3
MSC 74Q15

On analytical estimates of the effective elastic properties of polycrystalline silicon*

M. Aßmus, H. Altenbach

Otto von Guericke University,
2, Universitätsplatz, Magdeburg, 39106, Germany

For citation: Aßmus M., Altenbach H. On analytical estimates of the effective elastic properties of polycrystalline silicon. *Vestnik of Saint Petersburg University. Mathematics. Mechanics. Astronomy*, 2022, vol. 9 (67), issue 3, pp. 440–451. https://doi.org/10.21638/spbu01.2022.305

Several analytical approaches can be utilized to estimate the elastic properties of polycrystalline silicon. In experimental studies, the notion of an macroscopically isotropic aggregate is introduced while the single crystals obey cubic symmetry. We here give a synopsis on analytical approaches to predict elastic properties and apply them to estimate effective parameters of polycrystalline silicon. Here, the predictions are based on the parameters associated with shear solely. The results are juxtaposed in terms of the approaches applied, while different measures are introduced for evaluation. In comparison with experimental findings, the geometric mean implies a reasonable estimation for the elastic properties of polycrystalline silicon.

Keywords: silicon, cubic single crystals, polycrystalline aggregate, averaging methods, elasticity.

1. Introduction. Silicon has a large impact on todays world economy, aslo known as Silicon Age. For instance, it is an extremely important material for semiconductor electronics like photovoltaic cells where polycrystalline aggregates are primarily employed. For a safe and economic operation with this material, the most accurate prediction of the elastic properties possible is of interest. The problem of effective elastic parameters is also a question of material symmetry. The single crystals obey cubic symmetry while for the aggregate, the isotropy condition is reasonable, what is supported by experimental studies, e. g. [1]. However, the isotropic bulk properties of polycrystalline materials are homogenized values of their microconstituents.

Homogenization is commonly referred to as the calculation of the constitutive relationship between macroscopic field quantities — here stress and strain — as a function of material structure and material properties at the micro level. So first, effective dynamic and kinematic quantities have to be defined. In present case, the description can be restricted to linear elasticity where, based on Hill's theorem [2], the macroscopic strain energy is defined by the half of the product of volume averages of Cauchy stress tensor and infinitesimal strain tensor. Hence, the volume averages of stress and strain are considered as effective measures.

*This work was partially funded by the German Research Foundation (DFG) within the Research Training Group RTG 1554/II Micro-Macro-Interactions of Structured Media and Particle Systems (grant no. 83477795).

© St Petersburg State University, 2022

The mathematical description of polycrystalline microstructures is of fundamental importance for their analysis. On the one hand, the microstructure must be described locally, and on the other hand, a statistical description must be made based on the local one. The local description of microstructures is done by the aid of indicator functions. Such functions have the value 1 where the corresponding material is present, otherwise 0 [3]. For single-phased but polycrystalline materials, an indicator function is assigned to each crystal orientation [4]. The statistical description of the microstructure is based on the introduction of mean values of the indicator functions, which correspond to the volume fractions of the material belonging to the indicator function or the associated crystal orientation. The mean values of the indicator function provide the simplest description of the microstructure based on volume averages. Due to their simplicity, such approaches are very popular, cf. [5, 6]. Higher moments of the indicator functions yield correlation functions of the crystal orientations [7]. These correlation functions can be used to describe fundamental features: The microstructure is statistically homogeneous if the correlation function is translation invariant and statistically isotropic if the correlation function is also rotation invariant. Both, homogeneity and isotropy should be basic assumptions of the effective elastic properties to be determined for polycrystalline silion in present work.

The outline of present paper is as follows. First, we delineate the constitutive relations for the single crystal and the aggregate in Section 2. For silicon, the consideration of elastic behaviour at small deformations is sufficient. The consitutive measures of the symmetry classes used are given in a rational representation. As our aim is to present approaches to homogenization and since homogenization is a purely mathematical problem, we exploit the projector representation and use their advantages in mathematical handling for a compact description which is associated with the clear physical and mathematical interpretation. Significant elasticity parameters are visualized.

In Section 3 we give an overview on problem-specific, analytical approaches to predict effective material properties. We consider a single-phase polycrystalline material whose crystals are characterised by the crystal orientation and their elastic properties. The distribution function of crystal orientations satisfies the isotropy condition. In addition to classical and extended methods for determining bounds, unique estimates as well as purely empirical approaches, which are often used as standard approximations, are listed and compared. We refrain from detailed derivations of the respective approaches and concentrate on application and evaluation on the basis of the present problem. Fully analytic forms of the different constitutive tensors for the effective material have been worked out in the respective treatises cited. Thereby, literature is too vast for us to attempt anything that approximates a complete listing of references. Hence we are content to cite the major treatises to the respective approaches. However, in what follows we have brought the original descriptions in a form which is consistent with the notation used in present treatise. The advantages of such notation associated with the spectral decomposition of the elasticity tensor becomes obvious.

Section 4 is devoted to the application of the homogenization approaches surveyed. Effective medium estimates based on a well-known source of the silicon single crystals parameters are determined. Different measures are introduced to describe the scattering of the results due to the different approaches. Such an in-depth analysis is motivated by the quantification of theoretically admissible ranges of the effective behaviour with a perspective of possible experimental investigations. Finally, the estimates of the differnt approaches are compared and discussed.

The paper concludes with a summary of the results and the consequent implications.

Notation. A direct notation is preferred in present treatise. First-order tensors are denoted as bold minuscules (e. g. $\boldsymbol{a}$), second-order tensors as bold majuscules (e. g. $\boldsymbol{A}$), and fourth-order tensors as black-board bold majuscules (e. g. $\mathbb{A}$). The dyadic product and single scalar contractions are denoted like $(\boldsymbol{a}\otimes\boldsymbol{b}\otimes\boldsymbol{c}):(\boldsymbol{d}\otimes\boldsymbol{e}) = (\boldsymbol{b}\cdot\boldsymbol{d})(\boldsymbol{c}\cdot\boldsymbol{e})\boldsymbol{a}$. The superscript index $\top$ denotes the transpose of a tensor which is defined via $\boldsymbol{a}\cdot\boldsymbol{B}^\top\cdot\boldsymbol{c} = \boldsymbol{c}\cdot\boldsymbol{B}\cdot\boldsymbol{a}$ or $\boldsymbol{A}:\mathbb{B}^\top:\boldsymbol{C} = \boldsymbol{C}:\mathbb{B}:\boldsymbol{A}$. The components of a tensor are given with respect to the orthonormalized bases $\boldsymbol{e}_i$ or $\boldsymbol{g}_i$. We make use of Einstein's summation convention with implicit summation from 1 to 3 that appear pairwise in a product, e. g., the second-order identity tensor is given by $\boldsymbol{I} = \boldsymbol{e}_i\otimes\boldsymbol{e}_i$. The fourth-order identity tensor is given by $\mathbb{I} = \boldsymbol{e}_i\otimes\boldsymbol{e}_j\otimes\boldsymbol{e}_i\otimes\boldsymbol{e}_j$. We furthermore need the Transposer $\mathbb{T} = \boldsymbol{e}_i\otimes\boldsymbol{e}_j\otimes\boldsymbol{e}_j\otimes\boldsymbol{e}_i$ to build the symmetric part of fourth-order identity tensor $2\mathbb{I}^{\mathrm{sym}} = \mathbb{I}+\mathbb{T}$. The superscript index -1 denotes the inverse of a tensor, e. g., $\boldsymbol{A}\cdot\boldsymbol{A}^{-1} = \boldsymbol{I}$ holds for second-order tensors and $\mathbb{A}:\mathbb{A}^{-1} = \mathbb{I}^{\mathrm{sym}}$ for fourth-order tensors. Orthogonal tensor have the property $\boldsymbol{A}^{-1} = \boldsymbol{A}^\top$. The Rayleigh product is denoted by $\boldsymbol{A}\star\mathbb{B}^0 = \mathbb{B}$. It maps all basis vectors of $\mathbb{B}^0$ simultaneously without changing its components. We also make use of the Frobenius norm of fourth-order tensors which is induced by the scalar contractions $||\mathbb{A}|| = [\mathbb{A}::\mathbb{A}]^{1/2}$.

2. Constitutive relations of crystal and aggregate. Pure elastic behavior in context of small deformations is represented by Hooke's law[1]. This law is given as a linear mapping of the strains $\boldsymbol{E}$ onto the stresses $\boldsymbol{T}$:

$$\boldsymbol{T} = \mathbb{C}:\boldsymbol{E}. \tag{1}$$

Herein $\mathbb{C}$ is the fourth-order constitutive tensor, while $\boldsymbol{E}$ and $\boldsymbol{T}$ are second-order tensors for the linearized strains and the Cauchy stresses. By the aid of the spectral decomposition [10] we can write $\mathbb{C}$ in projector representation [11]:

$$\mathbb{C} = \sum_{\alpha=1}^{n}\lambda_\alpha\mathbb{P}_\alpha. \tag{2}$$

Herein n is the maximum number of eigenvalues. In the general case $n = 6$ holds [12]. Furthermore, $\lambda_\alpha > 0$ are eigenvalues and $\mathbb{P}_\alpha$ are eigenprojectors of $\mathbb{C}$. The inverse of such a constitutive tensor is determined by the inversion of the eigenvalues:

$$\mathbb{C}^{-1} = \sum_{\alpha=1}^{n}\frac{1}{\lambda_\alpha}\mathbb{P}_\alpha. \tag{3}$$

Silicon crystals obey cubic symmetry. In context of Eq. (3), $n = 3$ holds. The three distinct cubic eigenvalues are as follows:

$$\lambda_1^{\mathrm{c}} = C_{1111} + 2C_{1122}, \qquad \lambda_2^{\mathrm{c}} = C_{1111} - C_{1122}, \qquad \lambda_3^{\mathrm{c}} = 2C_{2323}. \tag{4}$$

The cubic eigenprojectors [11] are

$$\mathbb{P}_1^{\mathrm{c}} = \frac{1}{3}\boldsymbol{I}\otimes\boldsymbol{I}, \qquad \mathbb{P}_2^{\mathrm{c}} = \mathbb{D} - \mathbb{P}_1^{\mathrm{c}}, \qquad \mathbb{P}_3^{\mathrm{c}} = \mathbb{I}^{\mathrm{sym}} - \mathbb{D}, \tag{5}$$

[1] Hooke's original statement *Ut tensio sic vis* [8, p. 1] (from anagram CEIIINOSSSTTUV, cf. [9, p. 31]) means *as the extension, so the force.* This implies linearity but was a geometry-dependent version of what is today known as Hooke's law.

while

$$\mathbb{D} = \sum_{i=1}^{3} \boldsymbol{g}_i \otimes \boldsymbol{g}_i \otimes \boldsymbol{g}_i \otimes \boldsymbol{g}_i = \boldsymbol{Q} \star \mathbb{D}^0 \quad \text{with} \quad \mathbb{D}^0 = \sum_{i=1}^{3} \boldsymbol{e}_i \otimes \boldsymbol{e}_i \otimes \boldsymbol{e}_i \otimes \boldsymbol{e}_i \,, \tag{6}$$

is the anisotropic portion, $2\mathbb{I}^{\text{sym}} = \boldsymbol{e}_i \otimes \boldsymbol{e}_j \otimes (\boldsymbol{e}_i \otimes \boldsymbol{e}_j + \boldsymbol{e}_j \otimes \boldsymbol{e}_i)$ is the identity on symmetric second-order tensors, and $\boldsymbol{I} = \boldsymbol{e}_i \otimes \boldsymbol{e}_i$ is the identity on first-order tensors. Herein we make use of the lattice vectors $\boldsymbol{g}_i$ of the single crystal and the fixed sample basis $\boldsymbol{e}_i$. These base vectors are related via the versor $\boldsymbol{Q} \in \mathcal{SO}(3)$, i. e. $\boldsymbol{g}_i = \boldsymbol{Q} \cdot \boldsymbol{e}_i$.

For an isotropic approximation at aggregate level $n = 2$ holds [11]. We here make use of the superscript index $\circ$ for the description of isotropic parameters. The isotropic eigenvalues are given as

$$\lambda_1^\circ = 3K \qquad \text{and} \qquad \lambda_2^\circ = 2G\,. \tag{7}$$

The variables K and G are known as bulk and shear modulus. They are related to the engineering parameters Young's modulus Y and Poisson's ratio ν:

$$Y = \frac{9KG}{3K+G}, \qquad \nu = \frac{3K-2G}{2(3K+G)}. \tag{8}$$

The associated isotropic projectors are as follows [11]:

$$\mathbb{P}_1^\circ = \mathbb{P}_1^{\text{c}}, \qquad \mathbb{P}_2^\circ = \mathbb{I}^{\text{sym}} - \mathbb{P}_1^\circ. \tag{9}$$

To demonstrate directional dependencies for mono- and polycrystal, we here make use of three-dimensional elasticity bodies. Again, the difference in the constitutive measures introduced in preceding section is shown as follows:

$$\mathbb{C}^{\text{c}} = \lambda_1^{\text{c}}\mathbb{P}_1^{\text{c}} + \lambda_2^{\text{c}}\mathbb{P}_2^{\text{c}} + \lambda_3^{\text{c}}\mathbb{P}_3^{\text{c}}, \qquad \mathbb{C}^\circ = \lambda_1^\circ\mathbb{P}_1^\circ + \lambda_2^\circ\mathbb{P}_2^\circ. \tag{10}$$

There are only two characteristic parameters that allow a unique three-dimensional representation of the directional properties of the elastic behavior. These parameters are the Young's modulus Y and the bulk modulus K. Following [11], we can determine these parameters on the basis of an constitutive tensor $\mathbb{C}$ of arbitrary material symmetry in dependence of a direction $\boldsymbol{d}$, parametrized in spherical coordinates, cf. [13]:

$$Y(\boldsymbol{d}) = \left[\, (\boldsymbol{d} \otimes \boldsymbol{d}) : \mathbb{C}^{-1} : (\boldsymbol{d} \otimes \boldsymbol{d}) \,\right]^{-1}, \tag{11}$$

$$K(\boldsymbol{d}) = \left[\, 3\,\boldsymbol{I} \quad : \mathbb{C}^{-1} : (\boldsymbol{d} \otimes \boldsymbol{d}) \,\right]^{-1}. \tag{12}$$

For present material, i. e. cubic single crystal and isotropic aggregate, the directional dependence of both parameters is visualized in Fig. 1.

3. Analytical homogenization of polycrystal properties. The prediction of elastic properties is a long standing problem. Besides time-consuming computational homogenization methods, there are analytical methods that have found widespread application. We here summarize several analytical approaches appropriate for the determination of effective isotropic elastic properties of cubic silicon aggregates. These approaches typically result in bounds and estimates of the polycrystals effective behaviour. In the course

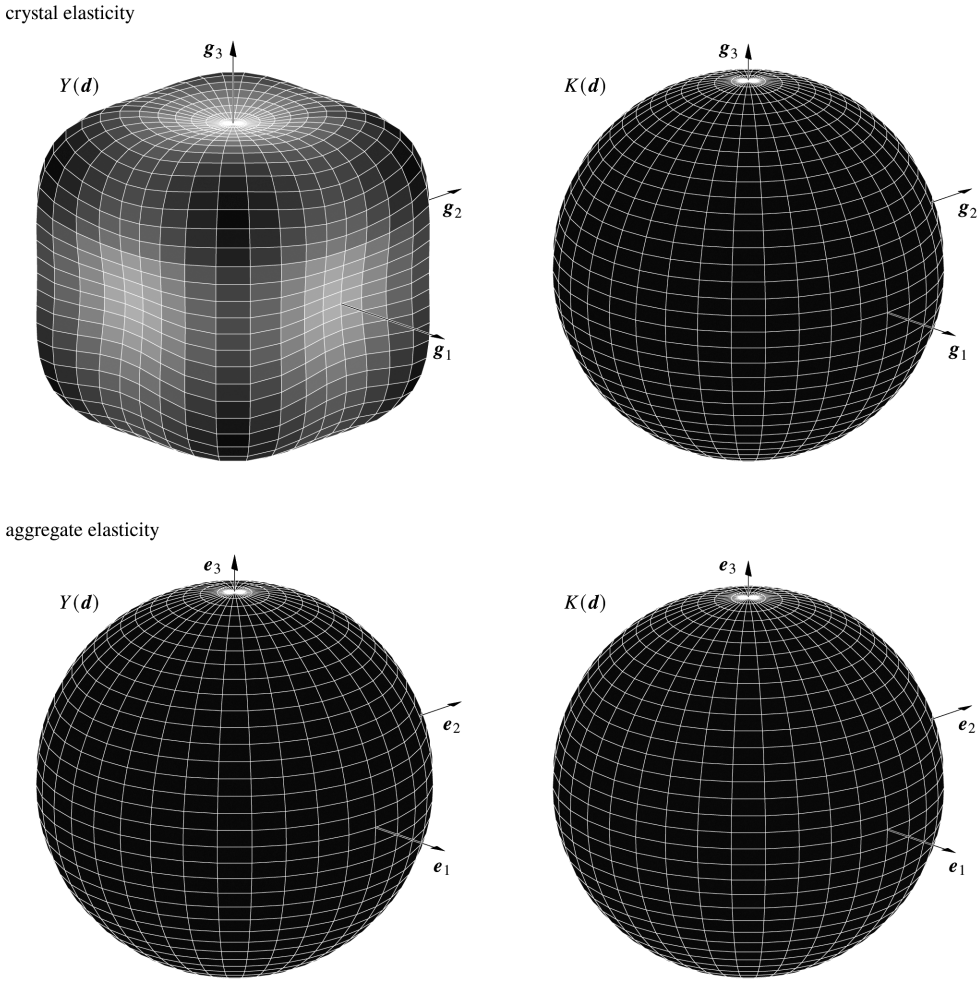

Fig. 1. Directional dependencies of Young's and bulk modulus for mono- (top) and polycrystalline (bottom) silicon.

of the specification of consitutive measures given in Section 2, subsequent description is based on operations with *cubic* eigenvalues. Due to the isotropic nature of volumetric changes, the bulk modulus is not subject to any modification from mono- to polycrystal. Thus, for all subsequent procedures, $\lambda_1^\circ = \lambda_1^\mathrm{c}$ holds, while λ_2° is sought, cf. Eq. $(10)_2$.

If we want to determine the elastic properties of the corresponding isotropic aggregate from components of the constitutive tensor of cubic single crystals, we have to statistically average over the orientation space. The early work on such procedures is due to Voigt and Reuss. Voigt [5] assumed that all crystals in a polycrystal have a uniform strain field. This results in a weighted sum of second and third eigenvalue:

$$\lambda_2^\mathrm{V} = \frac{2}{5}\lambda_2^\mathrm{c} + \frac{3}{5}\lambda_3^\mathrm{c}. \tag{13}$$

Reuss [6] assumed that all crystals in a polycrystal obey a uniform stress state. This results in a weighted sum of the reciprocals of the eigenvalues:

$$\lambda_2^{\mathrm{R}} = \frac{5\lambda_2^{\mathrm{c}}\lambda_3^{\mathrm{c}}}{2\lambda_3^{\mathrm{c}} + 3\lambda_2^{\mathrm{c}}}. \tag{14}$$

Aleksandrov and Aizenberg [14] proposed that the natural logarithm of the overall stiffness is equal to the average of the logarithms of the monocrystals stiffness. This results in an averaging scheme around the condition of the commutation of inverse and averaging operations:

$$\lambda_2^{\mathrm{A}} = (\lambda_2^{\mathrm{c}})^{2/5}(\lambda_3^{\mathrm{c}})^{3/5}. \tag{15}$$

This geometric mean has the powerful physical condition that the aggregate mean is equal to the mean of the inverse property.

The aforementioned eigenvalues are the arithmetic, the harmonic, and the geometric mean of the effective isotropic aggregate stiffness. The approaches by Voigt and Reuss constitute upper and lower bounds of the strain energy density [15]. Based on Jensen's inequality [16], for the relations to the geometric mean we can also state

$$\lambda_2^{\mathrm{V}} \geq \lambda_2^{\mathrm{A}} \geq \lambda_2^{\mathrm{R}}\,,$$

i. e., the eigenvalues based on the geometric mean are bounded by the those of the arithmetic and harmonic mean.

Hill [17] proposed two mean values of the bounds suggested by Voigt and Reuss. These are the arithmetic mean

$$\lambda_2^{\mathrm{H}+} = \frac{1}{2}\left[\lambda_2^{\mathrm{V}} + \lambda_2^{\mathrm{R}}\right]\,, \tag{16}$$

and the geometric mean

$$\lambda_2^{\mathrm{H}-} = \left[\lambda_2^{\mathrm{V}}\lambda_2^{\mathrm{R}}\right]^{1/2}\,. \tag{17}$$

Both parameters introduced above are purely empirical. Comparing Hill's proposals with Voigt and Reuss bounds, we can state

$$\lambda_2^{\mathrm{V}} \geq \lambda_2^{\mathrm{H}+} \geq \lambda_2^{\mathrm{H}-} \geq \lambda_2^{\mathrm{R}}\,.$$

Hashin and Shtrikman [18] proposed a variational principle to get tighter bounds compared to Voigt — Reuss bounds. In their approach, they relate quantities that represent a deviation from a reference solution. This approach is sketched in detailled manner in [19]. Subsequent eigenvalues result:

$$\lambda_2^{\mathrm{HS}+} = \lambda_3^{\mathrm{c}} + 2\left[\frac{5}{\lambda_2^{\mathrm{c}} - \lambda_3^{\mathrm{c}}} + \frac{6 \quad (\lambda_1^{\mathrm{c}} + 3\lambda_3^{\mathrm{c}})}{5\lambda_3^{\mathrm{c}}(\lambda_1^{\mathrm{c}} + 2\lambda_3^{\mathrm{c}})}\right]^{-1}, \tag{18}$$

$$\lambda_2^{\mathrm{HS}-} = \lambda_2^{\mathrm{c}} + 3\left[\frac{5}{\lambda_3^{\mathrm{c}} - \lambda_2^{\mathrm{c}}} + \frac{4 \quad (\lambda_1^{\mathrm{c}} + 3\lambda_2^{\mathrm{c}})}{5\lambda_2^{\mathrm{c}}(\lambda_1^{\mathrm{c}} + 2\lambda_2^{\mathrm{c}})}\right]^{-1}. \tag{19}$$

Comparing Hashin — Shtrikman bounds to the Voigt — Reuss bounds leads to the following relation:

$$\lambda_2^{\mathrm{V}} \geq \lambda_2^{\mathrm{HS}+} \geq \lambda_2^{\mathrm{HS}-} \geq \lambda_2^{\mathrm{R}}.$$

Huang [20] introduced a perturbation method to determine the effective elasticity tensor. For the special case of an isotropic orientation distribution, the estimate is determined as follow [21]:

$$\lambda_2^{\mathrm{Hg}} = \lambda_2^{\mathrm{V}} - \frac{12}{25}\frac{(\lambda_2^{\mathrm{c}} - \lambda_3^{\mathrm{c}})^2(5\lambda_1^{\mathrm{c}} + 6\lambda_2^{\mathrm{c}} + 9\lambda_3^{\mathrm{c}})}{(2\lambda_2^{\mathrm{c}} + 3\lambda_3^{\mathrm{c}})(5\lambda_1^{\mathrm{c}} + 4\lambda_2^{\mathrm{c}} + 6\lambda_3^{\mathrm{c}})}. \tag{20}$$

Fokin [22] proposed the singular approximation approach which is also based on a reference solution. This approach has been formulated for aggregates of cubic crystals by Matthies and Humbert [23]. In the case of an isotropic self-consistent solution, this approximation reduces as follows:

$$\lambda_2^{\mathrm{SA}} = \frac{2\lambda_2^{\mathrm{c}} p_2 + 3\lambda_3^{\mathrm{c}} p_3}{2p_2 + 3p_3}, \tag{21}$$

where the parameters p_γ are determined as follows:

$$p_\gamma = \left[1 + \frac{2}{5\lambda_2^{\mathrm{A}}}\frac{\lambda_1 + 3\lambda_2^{\mathrm{A}}}{\lambda_1 + 2\lambda_2^{\mathrm{A}}}(\lambda_\gamma^{\mathrm{c}} - \lambda_2^{\mathrm{A}})\right]^{-1} \qquad \forall\, \gamma = \{2, 3\}. \tag{22}$$

Based on aforementioned formulae it is possible to determine datasets of the isotropic effective aggregate behavior based on the single crystals cubic input data. This leads to isotropic effective aggregate stiffnesses for the respective homogenization approach:

$$\mathbb{C}^{\square} = \lambda_1 \mathbb{P}_1^{\circ} + \lambda_2^{\square} \mathbb{P}_2^{\circ} \qquad \forall\, \square \in \{\mathrm{V,\ R,\ A,\ H+,\ H\text{-},\ HS+,\ HS\text{-},\ Hg,\ SA}\}. \tag{23}$$

4. Results and discussion. We tabulate computed effective values of the elastic behavior of the silicon aggregate in Table. A visual counterpart can be found in Fig. 2. These effective outcomes are based on input given by Mason [24], i. e. $\lambda_1^{\mathrm{c}} = 293.50\,\mathrm{GPa}$, $\lambda_2^{\mathrm{c}} = 101.80\,\mathrm{GPa}$, and $\lambda_3^{\mathrm{c}} = 159.12\,\mathrm{GPa}$. Generally, we can identify the following relations:

• approaches based on Voigt and Reuss lead to outer bounds. All other estimates are within these extremes;

• Hashin — Shtrikman bounds considerably limit the range of feasible estimates compared to Voigt — Reuss bounds;

• estimates by Hill, Aleksandrov and Aizenberg, Huang, and the singular approximation approach lie in between the Hashin — Shtrikman bounds;

• Hill's estimates generate the lowest values within the Hashin — Shtrikman bounds;

• Huang's estimate generate the highest values within the Hashin — Shtrikman bounds;

• the estimate proposed by Aleksandrov and Aizenberg is located above Hill's estimates but below the singular approximation approach.

In addition, effective values discussed here are converted to engineering parameters which are presented in Fig. 4 of Appendix.

In summary, the first- (Voigt and Reuss) and second-order bounds (Hashin — Strikman) enclose the effective material behavior of the polycrystal. Thus, subsequent relations emerge for present input:

$$\lambda_2^{\mathrm{V}} > \lambda_2^{\mathrm{HS+}} > \lambda_2^{\mathrm{Hg}} > \lambda_2^{\mathrm{SA}} > \lambda_2^{\mathrm{A}} > \lambda_2^{\mathrm{H+}} > \lambda_2^{\mathrm{H-}} > \lambda_2^{\mathrm{HS-}} > \lambda_2^{\mathrm{R}}.$$

Estimates for an macroscopically isotropic silicon aggregate

$\lambda_\alpha^\square$	$\square$	$\alpha = 1$	$\alpha = 2$	mark
	V		136.19	▼
	R		129.87	▲
	A		133.09	◆
	H+		133.03	▼
[GPa]	H−	293.50	132.99	▲
	HS+		133.39	◆
	HS−		132.83	◆
	Hg		133.32	■
	SA		133.16	●

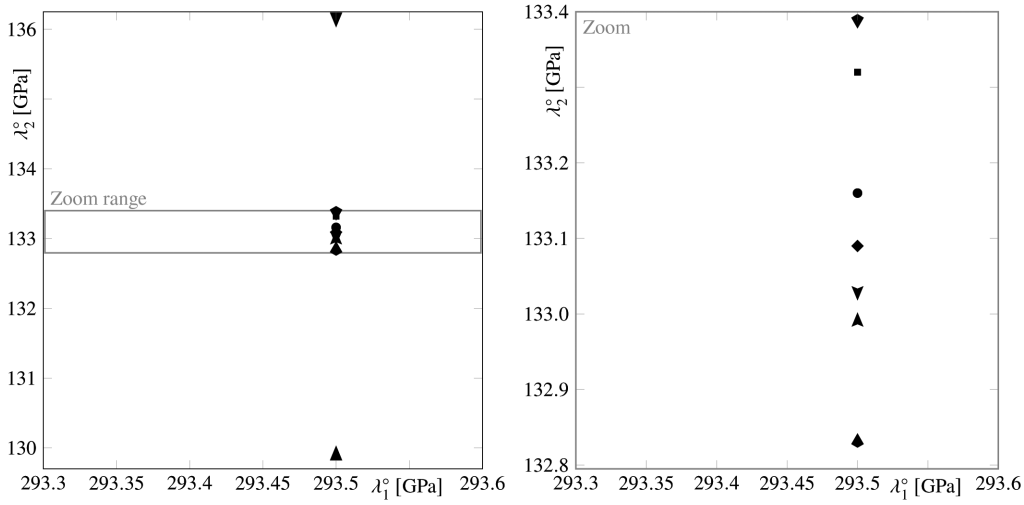

Fig. 2. Parameter space of analytically determined isotropic eigenvalues of the effective homogeneous medium.

This equivalently leads to the following bounds hierarchy to be understood in the spectral sense:

$$\mathbb{C}^{\mathrm{V}} > \mathbb{C}^{\mathrm{HS+}} > \mathbb{C}^{\mathrm{Hg}} > \mathbb{C}^{\mathrm{SA}} > \mathbb{C}^{\mathrm{A}} > \mathbb{C}^{\mathrm{H+}} > \mathbb{C}^{\mathrm{H-}} > \mathbb{C}^{\mathrm{HS-}} > \mathbb{C}^{\mathrm{R}}.$$

It is well known that the distance D^{VR} between Voigt and Reuss bounds increases with Zener's anisotropy ratio $ZR = \lambda_3^{\mathrm{c}}/\lambda_2^{\mathrm{c}}$:

$$D^{\mathrm{VR}} = \|\mathbb{C}^{\mathrm{V}} - \mathbb{C}^{\mathrm{R}}\| = \lambda_2^{\mathrm{c}} \frac{6\sqrt{5}(ZR-1)^2}{5(2ZR+3)}. \tag{24}$$

Since results based on the Hashin—Shtrikman approach present tighter bounds, we additionally introduce the distance D^{HS}:

$$D^{\mathrm{HS}} = \|\mathbb{C}^{\mathrm{HS+}} - \mathbb{C}^{\mathrm{HS-}}\|. \tag{25}$$

We can thus judge the bandwidth of the aggregate's elastic behavior. Results are depicted in Fig. 3 (left-hand side). As was to be expected, an improvement of the distance between upper and lower bounds in the degree of approximation order is evident. For present

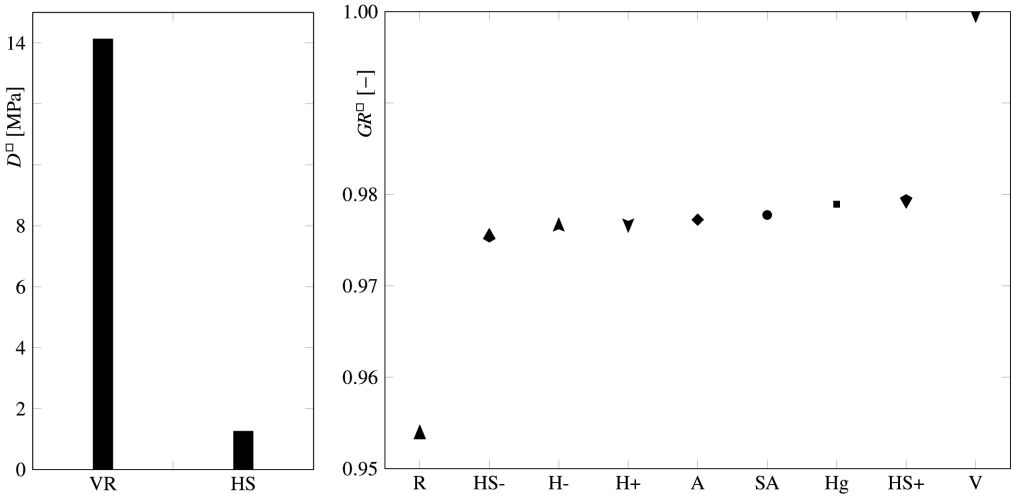

Fig. 3. Spanwidths of significant bounds and relative deviation of different estimates to the Voigt bound.

material $D^{\mathrm{HS}} \approx 8.9{\cdot}10^{-2} D^{\mathrm{VR}}$ results. This indicates that the Hashin — Shtrikman bounds are tighter by a factor of around 11 compared to Voigt — Reuss bounds, thus significantly diminish the domain of possible values.

As mentioned in Section 3, $\mathbb{C}^{\mathrm{V}}$ represents the upper bound of the elastic behavior. In the sequel we will hence normalize the homogenization results to this measure. More precisely, we reduce this normalization to the second isotropic eigenvalue λ_2^{V}. This restriction is possible since the first eigenvalue is the same for all approaches, cf. Table.

To judge the the scatter of the different estimates, we make use of the shear modulus ratio:

$$GR^{\square} = \frac{\lambda_2^{\square}}{\lambda_2^{\mathrm{V}}} = \frac{G^{\square}}{G^{\mathrm{V}}} \qquad \forall\, \square \in \{\mathrm{V,\ R,\ A,\ H+,\ H\text{-},\ HS+,\ HS\text{-},\ Hg,\ SA}\}. \tag{26}$$

Clearly, applying this scheme to the first eigenvalue, i. e. determining the bulk modulus ratio, will result in $KR = \lambda_1^{\square}/\lambda_1^{\mathrm{V}} = \kappa^{\square}/\kappa^{\mathrm{V}} = 1$ for any homogenization approach. When applying the normalization in Equation (26), all results depend on the isotropic eigenvalue ratio $LR^{\square} = \lambda_1^{\square}/\lambda_2^{\square}$ while Zener ratio remains $ZR \approx 1.56$ for present material. However, considering Fig. 3 (right-hand-side), it becomes evident that the effective estimates are at least 95.36 % of the Voigt bound. The Hashin — Shtrikman bounds lie inbetween 97.53 and 97.94 % of the upper bound. A comparison between Hashin — Shtrikman, Hill, Huang and self-consistent estimates shows that the geometric mean (97.72 % of the upper bound) provides an estimate pretty much in the middle of these predictions and very close to the self-consistent method (97.77 % of the upper bound) and Hill's arithmetic mean (97.67 % of the upper bound).

5. Summary and conclusions. The examination of the elastic properties of polycrystalline silicon has been carried out by using analytical estimates. A survey of approaches has been given being valid for isotropic aggregates of cubic crystals. The deviatoric portions of the single crystal constitutive tensor is used to form aggregate effective parameters. The estimates of the analytical approaches are appilied and compared.

It can be concluded that the scattering of the isotropic elastic properties of polycrystalline silicon due to the different approaches applied is comparatively small, at least within the Hashin — Shtrikman bounds. The reason for this is the comparatively low degree of ansiotropy of the silicon single crystal, cf. Zener ratio. Furthermore, present findings also imply that the choice of the geometric mean — a unique estimate for the effective elasticity tensor — is most consitent since it agrees quite well with the experimental findings, cf. Table 5 in [19]. Nevertheless, despite the lack of theoretical justification, Hill's arithmetic mean remains a useful estimate. However, since this requires the knowledge of the Voigt and Reuss bounds, the effort of computation is higher than directly determining the geometric mean.

In summary, the exploitation of such analytical approaches is much less time-consuming than applying finite-element computations and much more cost-efficient than conducting experiments.

6. Appendix. Extended results. Based on Table, it is also possible to give converted estimates of material parameters. We confine this conversion to Young's modulus and Poisson's ratio, cf. Eqs (7) and (8). The distribution of these parameters based on different estimates is visualized in Fig. 4.

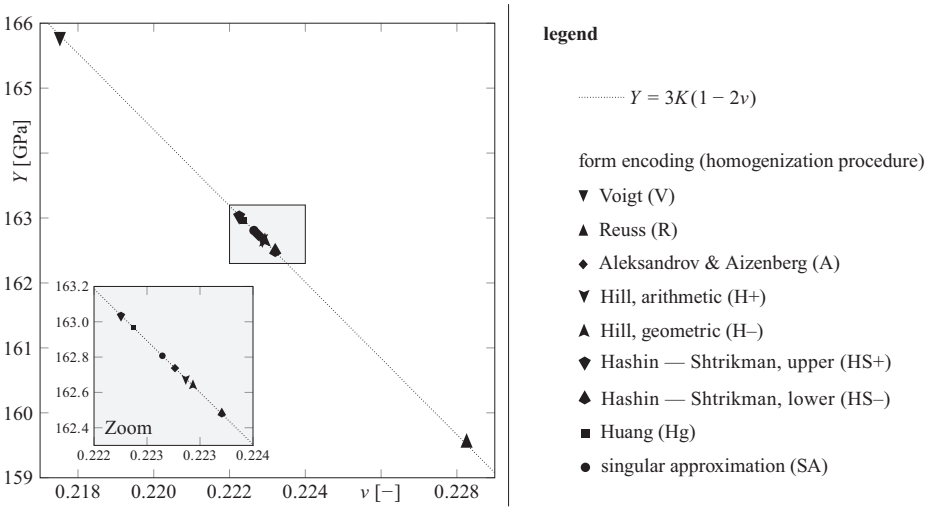

Fig. 4. Young's modulus and Poisson's ratio for different approaches.

All determined values lie on a straight between Voigt and Reuss bound. However, as given in Eq. (7), bulk and shear modulus are scaled parameters of the eigenvalues only, hence they are not depicted here.

References

1. Sharpe W. N. Mechanical Properties of MEMS Materials. In: M. Gad-el-Hak (ed.). *The MEMS Handbook*. CRC Press. Chapter 3, 1–33 (2002).

2. Hill R. On Constitutive Macro-Variables for Heterogeneous Solids at Finite Strain. *Proceedings of the Royal Society of London. Series A, Mathematical and Physical Sciences* **326** (1565), 131–147 (1972). Available at: http://www.jstor.org/stable/78044 (accessed: July 1, 2022).

3. Torquato S. *Random Heterogeneous Materials: Microstructure and Macroscopic Properties*. In Ser.: Interdisciplinary Applied Mathematics, vol. 16. New York, Springer (2002). https://doi.org/10.1007/978-1-4757-6355-3

4. Adams B., Olson T. The mesostructure-properties linkage in polycrystals. *Progress in Materials Science* **43** (1), 1–87 (1998). https://doi.org/10.1016/S0079-6425(98)00002-4

5. Voigt W. *Lehrbuch der Kristallphysik (mit Ausschluss der Kristalloptik)*. Wiesbaden, Springer (1910). https://doi.org/10.1007/978-3-663-15884-4

6. Reuss A. Berechnung der Fließgrenze von Mischkristallen auf Grund der Plastizitätsbedingung für Einkristalle. *Zeitschrift für Angewandte Mathematik und Mechanik* **9** (1), 49–58 (1929). https://doi.org/10.1002/zamm.19290090104

7. Beran M. *Statistical Continuum Theories. Monographs in statistical physics and thermodynamics*. Interscience Publishers (1968).

8. Hooke R. *De Potentia Restitutiva, or of Spring Explaining the Power of Springing Bodies*. London, John Martyn (1678). Available at: http://name.umdl.umich.edu/A44322.0001.001 (accessed: July 1, 2022).

9. Hooke R. *A Description of Helioscopes and Some other Instruments*. London, John Martyn (1676).

10 Halmos P. R. *Finite-Dimensional Vector Spaces*. New York, Springer (1958). https://doi.org/10.1007/978-1-4612-6387-6

11. Rychlewski J. Unconventional approach to linear elasticity. *Archives of Mechanics* **47** (5), 149–171 (1995).

12. Kowalczyk-Gajewska K., Ostrowska-Maciejewska J. Review on spectral decomposition of Hooke's tensor for all symmetry groups of linear elastic material. *Engineering Transactions* **57** (3-4), 145–1183 (2009). Available at: http://et.ippt.gov.pl/index.php/et/article/view/172 (accessed: July 1, 2022).

13. Nordmann J., Aßmus M., Altenbach H. Visualising Elastic Anisotropy: Theoretical Background and Computational Implementation. *Continuum Mechanics and Thermodynamics* **30** (4), 689–708 (2018). https://doi.org/10.1007/s00161-018-0635-9

14. Aleksandrov K. S., Aizenberg L. A. A method of calculating the physical constants of polycrystalline materials. *Doklady Akademii Nauk SSSR* **167** (5), 1028–1031 (1966). Available at: http://mi.mathnet.ru/eng/dan/v167/i5/p1028 (accessed: July 1, 2022). (In Russian)

15. Nemat-Nasser S., Hori M. *Micromechanics: Overall Properties of Heterogeneous Solids*. New York, Elsevier (1993).

16. Jensen J. L. W. V. Sur les fonctions convexes et les inégalités entre les valeurs moyennes. *Acta Mathematica* **30**, 175–193 (1906). https://doi.org/10.1007/BF02418571

17. Hill R. The Elastic Behaviour of a Crystalline Aggregate. *Proceedings of the Physical Society. Section A* **65** (5), 349–354 (1952). https://doi.org/10.1088/0370-1298/65/5/307

18. Hashin Z., Shtrikman S. A variational approach to the theory of the elastic behaviour of polycrystals. *Journal of the Mechanics and Physics of Solids* **10** (4), 343–352 (1962). https://doi.org/10.1016/0022-5096(62)90005-4

19. Aßmus M., Glüge R., Altenbach H. Hashin — Shtrikman Bounds of Cubic Crystalline Aggregate Elasticity for poly-Si Solar Cells. *Technische Mechanik* **41** (1), 24–33 (2021). https://doi.org/10.24352/ub.ovgu-2021-004

20. Huang M. Perturbation approach to elastic constitutive relations of polycrystals. *Journal of the Mechanics and Physics of Solids* **52** (8), 1827–1853 (2004). https://doi.org/10.1016/j.jmps.2004.02.006

21. Huang M., Man C.-S. Explicit Bounds of Effective Stiffness Tensors for Textured Aggregates of Cubic Crystallites. *Mathematics and Mechanics of Solids* **13** (5), 408–430 (2008). https://doi.org/10.1177/1081286507078299

22. Fokin A. G. Solution of statistical problems in elasticity theory in the singular approximation. *Journal of Applied Mechanics and Technical Physics* **13**, 85–89 (1972). https://doi.org/10.1007/BF00852360

23. Matthies S., Humbert M. On the Principle of a Geometric Mean of Even-Rank Symmetric Tensors for Textured Polycrystals. *Journal of Applied Crystallography* **28** (3), 254–266 (1995). https://doi.org/10.1107/S0021889894009623

24. Mason W. P. *Physical Acoustics and the Properties of Solids*. Princeton, New Jersey, D. Van Nostrand Co. (1958). Available at: https://hdl.handle.net/2027/mdp.39015006372356 (accessed: July 1, 2022).

Received: January 14, 2022
Revised: March 1, 2022
Accepted: March 3, 2022

Authors' information:

Marcus Aßmus — Dr Sci., Researcher; marcus.assmus@ovgu.de
Holm Altenbach — Dr Sci., Prof.; holm.altenbach@ovgu.de

Об аналитических оценках эффективных упругих свойств поликристаллического силикона*

М. Азмус, Х. Альтенбах

Университет им. Отто фон Герике, Германия, 39106, Магдебург, Университетская пл., 2

Для цитирования: *Aßmus M., Altenbach H.* On analytical estimates of the effective elastic properties of polycrystalline silicon // Вестник Санкт-Петербургского университета. Математика. Механика. Астрономия. 2022. Т. 9 (67). Вып. 3. С. 440–451.
https://doi.org/10.21638/spbu01.2022.305

Для оценки упругих свойств поликристаллического кремния можно использовать несколько аналитических подходов. В экспериментальных исследованиях вводится понятие макроскопически изотропного агрегата, когда монокристаллы подчиняются кубической симметрии. В статье дается краткий обзор аналитических подходов к прогнозированию упругих свойств и их применению для оценки эффективных параметров поликристаллического кремния. Прогнозы основаны исключительно на параметрах, связанных со сдвигом. Результаты сопоставляются для разных применяемых подходов, а для оценки вводятся различные меры. При сравнении с экспериментальными данными среднее геометрическое означает разумную оценку упругих свойств поликристаллического кремния.

Ключевые слова: кремний, кубические монокристаллы, поликристаллический агрегат, методы усреднения, эластичность.

Статья поступила в редакцию 14 января 2022 г.;
доработана 1 марта 2022 г.;
рекомендована к печати 3 марта 2022 г.

Контактная информация:

Азмус Маркус — marcus.assmus@ovgu.de
Альтенбах Хольм — holm.altenbach@ovgu.de

*Работа выполнена при частичной финансовой поддержке Немецкого исследовательского фонда в рамках Исследовательской учебной группы RTG 1554/II «Микро- и макровзаимодействия структурированных сред и систем частиц» (грант № 83477795).

UDC 539.42 Вестник СПбГУ. Математика. Механика. Астрономия. 2022. Т. 9 (67). Вып. 3
MSC 74R10

Fracture mechanics characterization of mortar nanocomposites reinforced with carbon nanotubes

E. Gdoutos[1], *M. Konsta-Gdoutos*[2]

[1] Academy of Athens,
28, Panepistimiou str., Athens, 106 79, Greece
[2] University of Texas at Arlington,
701, S. Nedderman Drive, Arlington, Texas, 76019, USA

For citation: Gdoutos E., Konsta-Gdoutos M. Fracture mechanics characterization of mortar nanocomposites reinforced with carbon nanotubes. *Vestnik of Saint Petersburg University. Mathematics. Mechanics. Astronomy*, 2022, vol. 9 (67), issue 3, pp. 452–463.
https://doi.org/10.21638/spbu01.2022.306

The objective of this paper is to provide a fracture mechanics characterization of mortar nanocomposites reinforced with multiwall carbon nanotubes (MWCNTs). The critical stress intensity factor, K_{Ic}, the strain energy release rate, G_{Ic}, the effective crack length, a_c, and the crack tip opening displacement, $CTOD_c$ are determined using three-point bend specimens. It was established that reinforcement of mortar with MWCNTs provides excellent improvement in the above fracture mechanics quantities.

Keywords: fracture mechanics, multi-wall carbon nanotubes, stress intensity factor, energy release rate, crack tip opening displacement, mortar nanocomposites, cementitious materials.

1. Introduction. Defects are of utmost importance in the mechanical and failure behavior of cementitious materials, like cement pastes, mortars, concrete, etc. These materials are heterogeneous with complex microstructure and can be modeled at various scale levels including the nano, micro, meso and macro levels. A simple way of modeling cementitious materials is to consider them as a two-phase particulate composite. In cement pastes the matrix is the hydrated cement gels and the reinforcement is the unhydrated cement particles. In mortar the matrix is the cement paste and the reinforcement is the fine aggregates. In concrete the matrix is the mortar and the reinforcement is the coarse aggregates.

Failure of cementitious materials is the result of initiation, growth and coalescence of defects, like pores, cracks, etc. starting from the nano, and progressing to micro, meso and macro scale levels. For example, in concrete microcracks are usually present, even before loading, at regions of high material porosity near the interfaces between the coarse aggregates and the mortar. Cracks may also be present in mortar. When the structure is subjected to applied loads, temperature difference, etc., both types of cracks start to increase and new cracks are formed. The interface cracks propagate into the mortar and are connected with the mortar cracks. When a sufficient number of microcracks coalesce a macrocrack is formed. The damage zone ahead of a traction free crack referred to as fracture process zone (FPZ) plays an important role in the analysis of growth of cracks.

© St Petersburg State University, 2022

Within the FPZ many failure mechanisms including microcracking, debonding of cement-matrix interface, crack deviation and branching take place. These mechanisms contribute to the energy of fracture. Carbon nanotubes (CNTs) with their supreme stiffness, high strength and aspect ratio are excellent reinforcing candidate materials, offering unprecedented improvement in both strength and stiffness [1, 2].

Attempts have been made to stop or delay the growth of cracks at micro and macro scale levels by reinforcing cementitious materials by fibers at these levels [3]. Microfibers are defined as fibers with diameters less than 50 μm and macrofibers with diameters less than 500 μm. Microfibers delay the process by which microcracks develop to form macrocracks by bridging the cracks and transfering the load, while macrofibers improve the post peak toughness of the material. Cracks, however, are formed at the nano scale level. To suppress the initiation and growth of these cracks, the use of nano fibers was introduced.

The superior mechanical, electrical and chemical properties of carbon nanotubes (CNTs) make them candidate materials for nano reinforcement. These materials, with aspect ratio greater than 1000 have Young's modulus around 1 TPa, tensile strength of 65–93 GPa, and maximum strain of 10–15 %. CNTs form agglomerates or bundles and adhere together with Van der Vaals forces which makes it particularly difficult to separate. Early attempts to add CNTs to cementitious materials have failed due to poor adhesion [4–10].

Konsta — Gdoutos and coworkers [1, 11–13] developed a revolutionary method for effective dispersion of CNTs in cement pastes, mortars and concrete. The dispersion of different lengths of multi-wall carbon nanotubes (MWCNs) in water was achieved by applying ultrasonic energy and using a surfactant. They studied the effects of ultrasonic energy and surfactant concentration on the dispersion of CMTs and concluded that an optimum of weight ratio of surfactant to CNTs should exist. They found that small amounts of effectively dispersed MWCNs (0.025–0.08 wt % of cement) increase the flexural strength of cementitious composites. Furthermore, they studied the effect of carbon nanofibers (CNFs) and showed that the nanocomposites exhibit superior mechanical and electromechanical properties. They demonstrated that CNFs and carbon fibers (CFs) can be used in concrete to successfully create a conductive network for stress/damage detection. They found that in cement nanocomposites reinforced with MWCNs the modulus of elasticity increases by 45 % with respect to the cement paste material, while the flexural strength increases by 25 % for a reinforcement of 0.08 wt %. Moreover, they established that longer MWCNTs are more effective than shorter ones.

In the above works the effect of MWCNTs and CNTs on the Young's modulus, strength and ductility of cementitious material was studied. However, fracture mechanics characterization of cementitious material requires determination of critical fracture mechanics quantities including stress intensity factor, K_I, critical strain energy release rate, G_I, critical crack mouth opening displacement, $CMOD_c$ and critical crack length, a_c. Failure by crack propagation can be described when stress intensity factor, strain energy release rate or crack mouth opening displacement reach their critical values. These quantities are functions of applied loads and the size and dimensions of the structure, while their critical values are material properties.

The foundations of the application of fracture mechanics to concrete were laid down by the pioneering work of Hillerborg [14, 15] who introduced the fictitious crack model of concrete, in an analogous way to the Dugdale — Barenblatt model of metals. After that, the development of the field was explosive and the theory appears to be matured for

applicability to design. Early works on the application of fracture mechanics to concrete are listed in references [16–27]. Reda et al. [28] used the effective crack model developed by Karihaloo and Nallathambi [29] to determine the critical energy release rate for high performance concrete, mortar, fiber reinforced concrete and masonry units. Moukwa et al. [30] studied the effect of alumino-silicate clays on the critical stress intensity factor and critical crack tip opening displacement. They concluded that appropriate use of silica fume and alumino-silicate clays can increase the ductility and strength of cementitious materials. Das et al. [31] used notched three-point bend specimens to determine the critical stress intensity factor and critical crack tip opening displacement in mortars in which the Ordinary Portland Cement (OPC) was replaced by limestone or a combination of limestone and fly ash/metakaolin. The fracture quantities were determined by using a two-parameter method and a non-contact digital image correlation. It was obtained that blends of OPC replacement materials and limestone can lead to enhanced fracture mechanics properties and ductility. Sarker et al. [32] studied the fracture characteristics of geopolymer (GPC) and OPC concrete using three-point bend specimens. They found that the critical stress intensity factor is higher for the GPC than the OPC concrete. Nikbin et al. [33] studied the fracture characteristics of self-compacting concrete using notched three-point bend specimens. Stynoski et al. [34] studied the fracture properties of various Portland cement mixtures containing silica fume, carbon nanotubes and carbon nanofibers using notched three-point bend specimens and the two-parameter method of Jenq and Shah [2]. They found an improved fracture mechanics performance of mixtures containing carbon nanotubes and carbon nanofibers.

It is the objective of the present work to characterize the fracture mechanics behavior of cementitious materials reinforced with well-dispersed carbon nanotubes. Experiments were performed on three-point bending precracked specimens of cement pastes without and with MWCNTs reinforcement. The excellent reinforcing capabilities of MWCNTs are demonstrated by a significant improvement in critical stress intensity factor (128.6 %), critical strain energy release rate (154.9 %), critical crack tip opening displacement (39.7 %) and effective crack length (10.3 %), resulting in advanced materials for civil engineering applications.

2. Fracture mechanics of cementitious materials. Fracture mechanics characterization of cementitious materials, like cement pastes, mortars and concretes is important for various reasons. First, it is generally accepted that material separation is better described by energy principles rather than by stress or strain. During fracture, new material surfaces are created. The energy required to create new material surfaces during the fracture process is a fundamental characteristic quantity of the material. Application of fracture mechanics gives a basis for the understanding of the fracture process. Second, high strength concrete with compressive strength higher than 100 N/mm^2 presents extremely brittle behavior, and fracture mechanics is well suited for studying its failure. Third, design of large structures, like dams, nuclear reactors, behave in a rather brittle manner, and their design will be benefited tremendously by fracture mechanics. Fourth, characterization of fracture toughness by the area under the stress-strain curve of the material cannot be used to quantify fracture toughness, since it is size and geometry dependent. Fifth, classical theories of fracture based on stress or strain cannot explain the size effect, according to which the ultimate stress of geometrically similar structures of different sizes depends on the size of the structure. The size effect can only be explained by fracture mechanics.

Direct application of fracture mechanics to cementitious materials is questionable, since the values of the critical strain energy release rate are specimen size dependent and, therefore, they could not be used as a characteristic material property. It was realized that cementitious materials require a different kind of fracture mechanics than metals. In both metal and concrete structures, nonlinear zones of small (small scale yielding approximation treated by linear elastic fracture mechanics) or normal sizes (ductile fracture) develop at the crack tip. However, in ductile/brittle metals the material in the nonlinear fracture process zone ahead of the crack tip undergoes hardening or perfect plasticity, whereas in concrete the material undergoes softening damage. In cementitious materials within the fracture process zone (FPZ) many micro-failure mechanisms including matrix microcracking, debonding of cement-matrix interface, crack deviation and branching take place. All these mechanisms contribute to the energy of fracture. The size of the fracture process zone ahead of the stress-free crack depends on the geometry and size of the structure and the type of material. For cement paste the length of the FPZ is of the order of a millimeter, for mortar is about 30 mm, for normal concrete of course-grained rock is up to 500 mm, for dam concrete with extra-large aggregates is about 3 m, for a grouted soil mass is around 10 m and in a mountain and jointed rock values of 50 m may be typical. On the other hand the length of the FPZ in a fine-grained silicon ozide ceramic is of the order of 0.1 mm, and in a silicon wafer of the order of 10–100 nm.

3. Experimental determination of K_{Ic}, G_{Ic} and $CMOD_c$. ***3.1. General remarks.*** Direct application of fracture mechanics principles have been used for the experimental determination of the critical fracture toughness of cementitious materials. The methodology has been similar to the experimental determination of the critical strain energy release rate, G_{Ic}, or stress intensity factor, K_{Ic}, in metals. Notched three-point bend specimens have been most popular. The specimens were loaded to a progressively increasing load and the load versus deflection of crack tip opening displacement response was recorded. The value of G_{Ic}, or K_{Ic}, is determined from the peak load or the load at the intersection with the secant of slope 95 % of the initial slope with the load-displacement curve. The values of G_{Ic}, or K_{Ic} obtained were dependent on the size of the specimen and its geometrical configuration. Thus direct application of linear elastic fracture mechanics for the characterization of the fracture behavior of cementitious materials is not successful.

3.2. The Jenq — Shah method. In an effort to provide reliable critical fracture toughness values of cementitious materials, Jenq and Shah [2] proposed a methodology based on the compliance of the notched specimen. The basic idea behind the method is to determine an effective, not the initial, crack length. This effective crack length takes into consideration the inelastic phenomena that take place in the fracture process zone ahead of the crack tip. The effective crack length is equal to the actual crack length plus the length of the fracture process zone. For the application of the method the relationship between the compliance, defined as the value of the crack tip opening displacement per unit load, and the crack length for special specimen types (three-point notched bend specimen) is established. The unloading compliance of the specimen is determined by unloading the specimen after reaching the peak load. The effective crack length is calculated from the relationship between the compliance and the crack length using the unloading compliance. The critical value of strain energy release rate, G_{Ic}, or stress intensity factor, K_{Ic}, is calculated from the peak load and the effective crack length using linear elastic fracture mechanics formulas. It has been established that K_{Ic}

determined in this way is independent of the specimen type and size. Thus, determination of K_{Ic} needs two quantities measured from the test, the unloading compliance and the peak load. Simultaneously with K_{Ic} the modulus of elasticity and the critical value of the crack tip opening displacement are determined.

The experimental determination of the above quantities is based on the load versus crack mouth opening displacement (CMOD) curve for a loading-unloading cycle of a three-point bend specimen (Fig. 1).

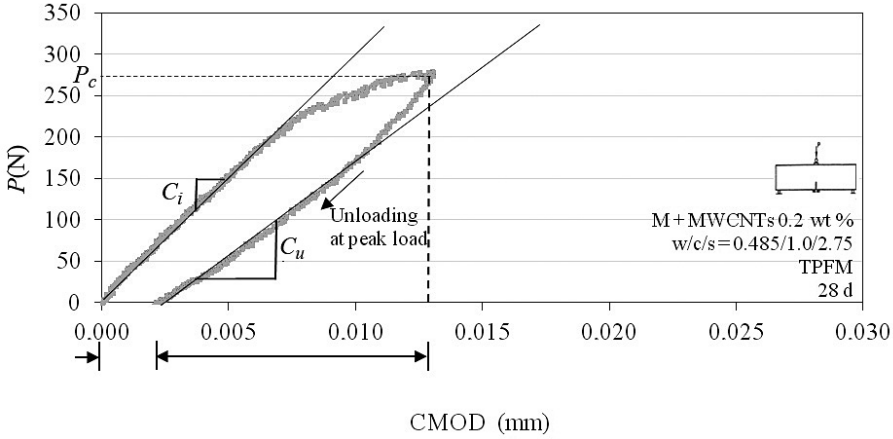

Fig. 1. Typical load-CMOD curve from loading and unloading procedure for 28 d mortar reinforced with well dispersed MWCNTs at an amount of 0.2 wt % of cement.

From the curve the following quantities are measured: the compliances for the loading and unloading parts and the maximum load.

The modulus of elasticity, E, is calculated by

$$E = \frac{6Sa_0 g_2(\alpha_c)}{C_i b^2 t}, \tag{1}$$

where C_i — the compliance of the loading part of the load-CMOD curve, $\alpha_c = (a_0 + HO)/(b + HO)$, a_0 is the crack length, S is the span length, b is the specimen depth, t is the specimen thickness, HO is the length defined in Fig. 2, between the two mark points on the bottom of the beam, $g_2(\alpha_0)$ — geometric function defined by

$$g_2(\alpha_0) = 0.76 - 2.28\alpha_0 + 3.87\alpha_0^2 - 2.04\alpha_0^3 + \frac{0.66}{(1-\alpha_0)^2}. \tag{2}$$

In a similar way, the modulus of elasticity E is calculated from the compliance of the unloading part of the load-CMOD curve as

$$E = \frac{6Sa_c g_2(\alpha_0)}{C_u b^2 t}, \tag{3}$$

where C_u is the compliance of the unloading part of the load-CMOD curve, a_c is the effective crack length, $\alpha_c = (a_c + HO)/(b + HO)$.

The unloading compliance is taken within 95 % of the peak load calculated from the load-CMOD curve. The value of the effective crack length a_c is calculated by equating

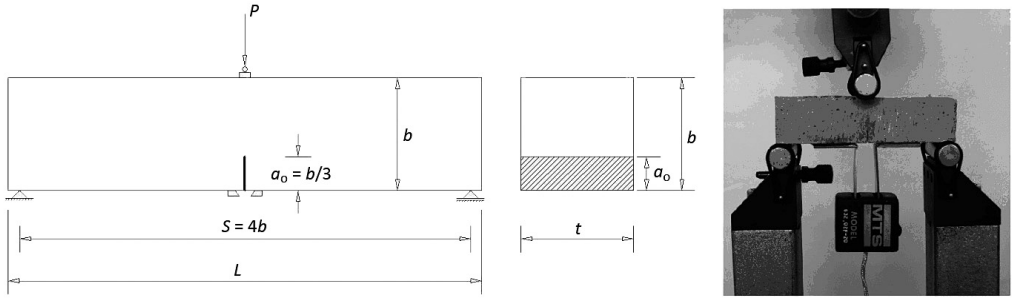

Fig. 2. Experimental setup for the TPFM testing.

the values of the modulus of elasticity E defined from Eqs (1) and (3). This results in the following equation

$$a_c = a_0 \frac{C_u}{C_i} \frac{g_2(\alpha_0)}{g_2(\alpha_c)}. \tag{4}$$

Equation (4) is solved numerically for the determination of the critical crack length a_c.

The critical stress intensity factor is calculated by the equation

$$K_{IC}^S = 3(P_{cr} + W_h) \frac{S\sqrt{\pi a_c} g_1(a_c/b)}{2b^2 t}, \tag{5}$$

where P_{cr} is the peak load, $W_h = W_{ho} S/L$, W_{ho} is the self weight of the beam, and

$$g_1\left(\frac{a_c}{b}\right) = \frac{1.99 - (a_c/b)(1 - a_c/b)[2.15 - 3.93(a_c/b) + 2.70(a_c/b)^2]}{\sqrt{\pi}(1 + 2a_c/b)(1 - a_c/b)^{3/2}}. \tag{6}$$

The critical crack tip opening displacement is calculated by

$$CTOD_c = \frac{6(P_c + 0.5W_h) S a_c g_2(a_c/b)}{E b^2 t} [(1-\beta_0)^2 + (1.081 - 1.149(a_c/b))(\beta_0 - \beta_0^2)]^{1/2}, \tag{7}$$

where $\beta_0 = a_0/a_c$, $g_2(a_c/b)$ is calculated from Eq. (2) with $\alpha_0 = a_c/b$.

Based on the values of K_{Ic}^s and $CMOD_c$ Jenq and Shah [2] introduced a material length Q by

$$Q = \left(\frac{E\, CTOD_c}{K_{Ic}^s}\right)^2. \tag{8}$$

The material length Q can be used to characterize the brittleness of the material. The smaller the value of Q and more brittle the material is. It was found that values of Q are in the range of 12.5–50 mm for hardened cement paste, 50–150 for mortar, and 150–350 for concrete.

4. Experimental work. ***4.1. Materials and specimens.*** The material investigated in this work was a cement-based composite with the matrix reinforced by multi-walled carbon nanotubes (MWCNTs). The nanotube reinforcement was of 10–100 μm length and 20–40 nm outer diameter. Characteristic properties of MWCNTs and are shown in Table 1.

Type I ordinary Portland cement (OPC) and standard sand according to EN 196–1 were used for casting the cement paste and mortar specimens. To disperse the MWCNTs

Table 1. **Properties of MWCNTs**

Nanotubes	Diameter, nm	Length, μm	Surface area, m^2/gr	Bulk density, gr/cm^3	Aspect ratio
MWCNTs	20–45	≥ 10	> 200	≤ 0.18	500

homogeneously in the mixing water, MWCNT suspensions were prepared by adding the MWCNTs in an aqueous surfactant solution that includes a commercially available polycarboxylate based surfactant (SFC). The resulting dispersions were sonicated at room temperature following the method described by Konsta-Gdoutos et al. [11, 12]. A constant surfactant to MWCNTs weight ratio of 4.0 was found to achieve effective dispersion. Ultrasonic energy is applied to the aqueous samples by a 500 W cup-horn high intensity ultrasonic processor with a standard probe of a diameter of 13 mm and temperature controller. The sonicator is operated at amplitude of 50 % so as to deliver constant energy rate of 1900–2100 J/min, at cycles of 20 seconds in order to prevent overheating of the suspensions.

After completion of the sonication procedure, the MWCNT suspensions were added into the OPC and sand at a constant water to cement ratio $w/c = 0.485$ and sand to cement ratio $s/c = 2.75$. Mixing of the materials was performed according to procedure outlined by ASTM 305 using a standard robust mixer capable of operating from 140 ± 5 to 285 ± 10 revolutions per minute (r/min). After mixing, one set of the mixture was cast in $20 \times 20 \times 80$ mm oiled molds. Following demolding, the samples were cured in lime-saturated water until testing. A 6 mm notch was introduced into the prismatic $20 \times 20 \times 80$ mm specimens using a water-cooled band saw machine.

The same procedure was used for both cement pastes and mortars. Values of an estimated number of nanotubes per unit volume of the cementitious matrix are also included in the Table 2, expressed as MWCNT count.

Table 2. **Fiber count of MWCNTs in the cementitious matrix**

	Fiber count
M	—
M + MWCNTs 0.1 wt %	36.1×10^{10}
M + MWCNTs 0.2 wt %	72.2×10^{10}

4.2. Testing procedure. Prismatic notched specimens $20 \times 20 \times 80$ mm were tested in three point bending at ages of 3, 7 and 28 days. The test was performed using a 25 kN MTS servo-hydraulic, closed-loop testing machine. The specimens were tested in a crack mouth opening displacement (CMOD)-controlled mode. The CMOD was used as the feedback signal to produce stable crack propagation at the rate of 0.008 mm/min, such that the peak load is reached in about 5 min. The prismatic specimens were monotonically loaded up to the maximum load. The applied load is then manually reduced after the load passed the maximum load and within the 95 % of the maximum load.

The two-parameter method [2] was used to obtain the fracture mechanics properties of the specimens from the experimental results. These properties include the critical stress intensity factor, K_{Ic}^S, the critical strain energy release rate, G_{Ic}^S, the critical crack

tip opening displacement, $CTOD_c$, and the critical crack length, a_c. For the application of the method the loading and unloading compliances and the peak load were monitored during the test. A typical loading-unloading load-CMOD curve of a mortar nanocomposite reinforced with well dispersed MWCNTs at an amount of 0.2 wt % of cement is shown in Fig. 1. According to the ASTM C348, specimens of strengths deviating by more than 10 % of the average strength were discarded. The three-point bend specimen geometry and experimental setup is shown in Fig. 2.

5. Results and discussions. A series of experiments were performed to determine fracture mechanics parameters including critical stress intensity factor, K_{Ic}^S, critical strain energy release rate, G_{Ic}^S, critical crack tip opening displacement $CTOD_c$ and effective crack length a_c in notched three-point bend specimens. Specimens of neat mortar and mortar reinforced with MWCNTs at amounts of 0.10 and 0.20 wt % were performed. Fig. 3 presents the variation of K_{Ic} versus time for up to 28 days for neat mortar and mortar reinforced with MWCNTs at amounts of 0.1 and 0.2 wt % of cement.

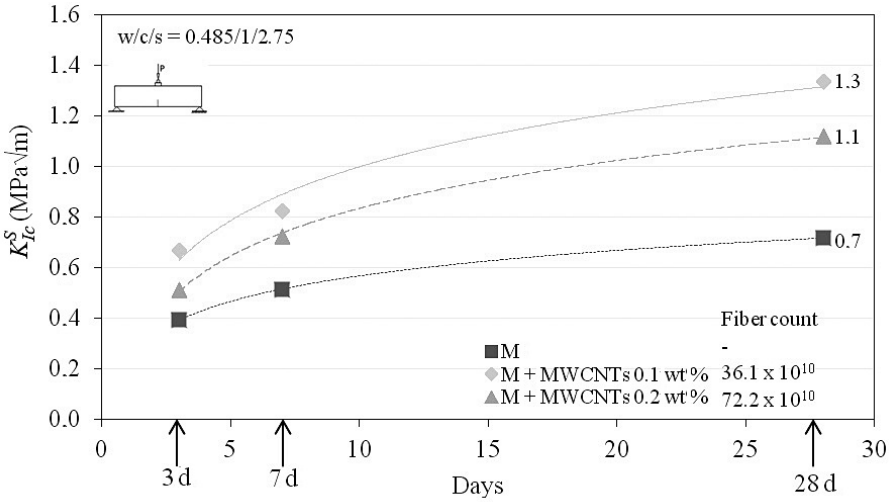

Fig. 3. Critical stress intensity factor, K_{Ic}, of neat mortar and mortar reinforced with MWCNTs at amounts of 0.1 and 0.2 wt % of cement versus time for up to 28 days.

The water to cement to sand ratio was w/c/s = 0.485/1/2.75. Note that K_{Ic} increases with time for all three cases. K_{Ic} also increases with the addition to neat mortar of MWCNTs. However, values of K_{Ic} are higher for an addition of 0.1 wt % than an addition of 0.2 wt % MWCNs. This behavior can be attributed to poor dispersion of MWCNTs in mortar as their percentage increases. Analogous results for the critical strain energy release rate, G_{Ic}, are shown in Fig. 4.

Results for the critical crack tip opening displacement, CTODc, at 28 days for mortars reinforced with MWCNs at amounts of 0.1 and 0.2 wt % are shown in Fig. 5.

Note that $CTOD_c$ at 0.1 wt % is higher than at 0.2 wt %. The bars in the figure indicate the error in the determination of $CTOD_c$. Finally, Fig. 6 presents results for the material length Q of 28 day neat mortar and mortars reinforced with 0.1 and 0.2 wt % of cement.

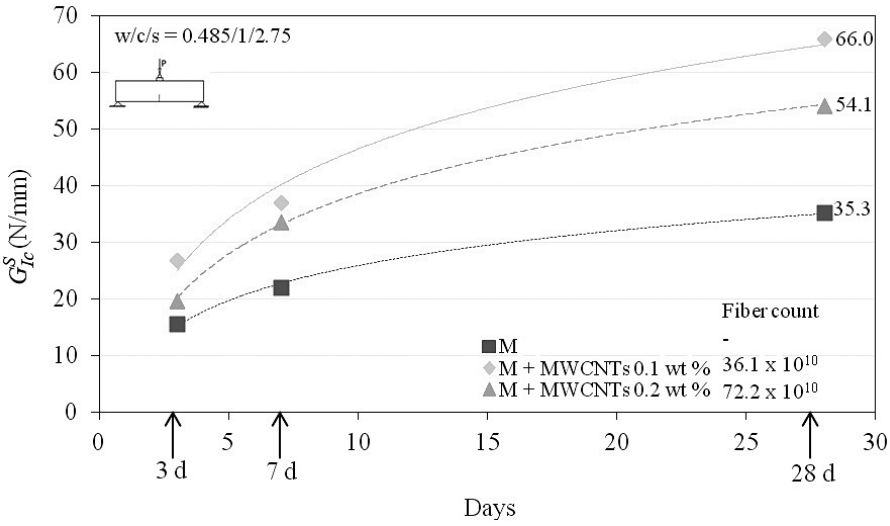

Fig. 4. Strain energy release rate of neat mortar and mortars reinforced with MWCNTs at amounts of 0.1 and 0.2 wt % of cement up to 28 days of hydration.

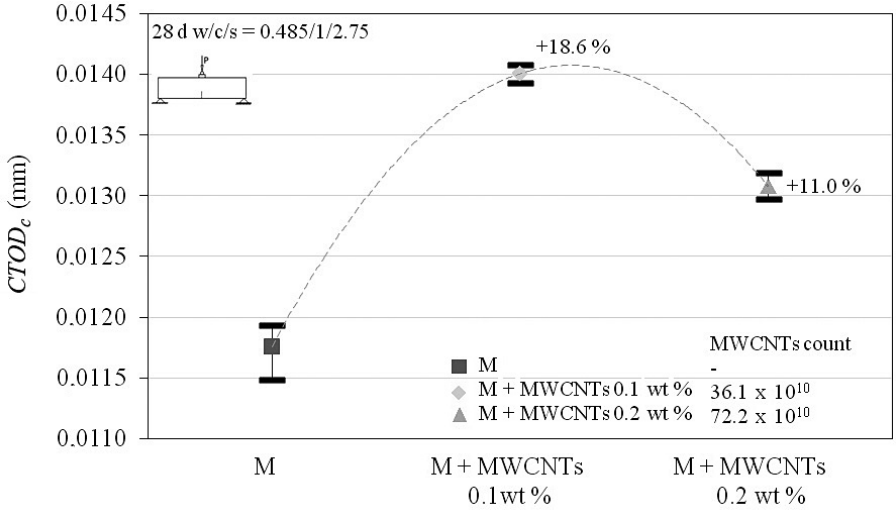

Fig. 5. Critical crack tip opening displacement of 28 days neat mortar and mortars reinforced with 0.1 and 0.2 wt % of cement MWCNTs.

6. Conclusions. A thorough study of the effect of reinforcement of neat mortar with multiwall carbon nanotubes (MWCNTs) at amounts of 0.1 and 0.2 wt % on the fracture behavior of the nanocomposite was conducted. Fracture properties measured include critical stress intensity factor, critical strain energy release rate, critical crack tip opening displacement and effective crack length. All these quantities were substantially increased by addition of MWCNTs and CNFs. Previous results [11–13] have demonstrated the beneficial effect of enhancement of tensile strength and Young's modulus of cement pastes, mortars and concrete reinforced with small amounts of MWCNTs and CNFs.

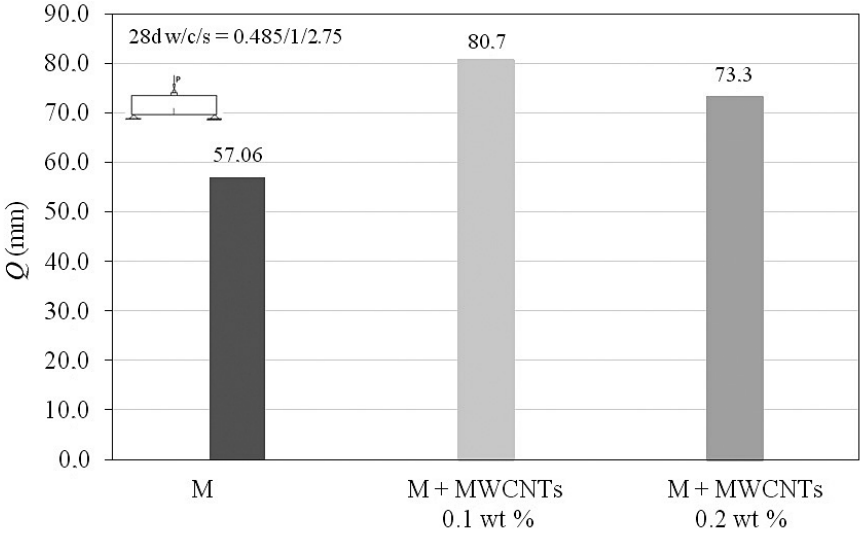

Fig. 6. Material length Q of 28 day neat mortar and mortars reinforced with 0.1 and 0.2 wt % of cement.

The main results of the present study referring to reinforcing capabilities of MWCNTs and CNFs at amounts of 0.1 and 0.2 wt % on the fracture properties of mortars may be summarized as:

(i) the critical stress intensity factor increases by an amount of 128.6 %;

(ii) the critical strain energy release rate increases by an amount of 154.9 %;

(iii) the critical crack tip opening displacement increases by an amount of 39.7 %;

(iv) the effective crack length increases by an amount of 10.3 %;

(v) reinforcement of mortars by adding MWCNs at amount of 0.1 % is more effective than adding MWCNs at amount of 0.2 %. This behavior can be attributed to the poor dispersion of MWCNs at higher concentrations.

This paper is dedicated to Professor Nikita Fedorovich Morozov on the occasion of his 90th birthdate. We wish our friend Nikita many more blessed years with good health, happiness and productivity.

References

1. Konsta-Gdoutos M. S., Metaxa Z. S., Shah S. P. Highly dispersed carbon nanotubes reinforced cement based materials. *Cem. Concr. Res.* **40**, 1052–1059 (2010). https://doi.org/10.1016/j.cemconres.2010.02.015

2. Jenq Y., Shah S. P. Two parameter fracture model for concrete. *J. Eng. Mech.* **111**, 1227–1241 (1985).

3. Akkaya Y., Shah S. P., Ghandehari M. Influence of fiber dispersion on the performance of microfiber reinforced cement composites. In: *ACI Special Publications 216: Innovations in Fiber-Reinforced Concrete for Value*, SP-216-1, vol. 216, 1–18 (2003).

4. Makar J. M., Margeson J., Luh J. Carbon nanotube/cement composites — early results and potential applications. *Proceedings of the 3rd International Conference on Construction Materials: Performance, Innovations and Structural Implications.* Canada, Vancouver, B. C., 1–10 (2005).

5. Li G. Y., Wang P. M., Zhao X. Mechanical behavior and microstructure of cement composites incorporating surface-treated multi-walled carbon nanotubes. *Carbon* **43** (6), 1239–1245 (2005). https://doi.org/10.1016/j.carbon.2004.12.017

6. Li G. Y., Wang P. M., Zhao X. Pressure-sensitive and microstructure of carbon nanotube reinforced cement composites. *Cem. Concr. Comp.* **29** (5), 377–382 (2007). https://doi.org/10.1016/j.cemconcomp.2006.12.011

7. Saez de Ibarra Y., Gaitero J. J., Erkizia E., Campillo I. Atomic force microscopy and nanoindentation of cement pastes with nanotube dispersions. *Physica Status Solidi (a)* **203** (6), 1076–1081 (2006). https://doi.org/10.1002/pssa.200566166

8. Wansom S., Kidner N. J., Woo L. Y., Mason T. O. AC-impedance response of multi-walled carbon nanotube/cement composites. *Cem. Concr. Comp.* **28** (6), 509–519 (2006). https://doi.org/10.1016/j.cemconcomp.2006.01.014

9. Cwirzen A., Habermehl-Chirzen K., Penttala V. Surface decoration of carbon nanotubes and mechanical properties of cement/carbon nanotube composites. *Adv. Cem. Res.* **20** (2), 65–73 (2008). https://doi.org/10.1680/adcr.2008.20.2.65

10. Xie X. L., Mai Y. W., Zhou X. P. Dispersion and alignment of carbon nanotubes in polymer matrix: a review. *Mater. Sci. Eng. Rep.* **49** (4), 89–112 (2005). https://doi.org/10.1016/j.mser.2005.04.002

11. Konsta-Gdoutos M. S., Metaxa Z. S., Shah S. P. Multi-scale mechanical and fracture characteristics and early-age strain capacity of high performance carbon nanotube/cement nanocomposites. *Cem. Concr. Compos.* **32** (2), 110–115 (2010). https://doi.org/10.1016/j.cemconcomp.2009.10.007

12. Metaxa Z. S., Konsta-Gdoutos M. S., Shah S. P. Carbon nanofiber cementitious composites: effect of debulking procedure on dispersion and reinforcing efficiency. *Cem. Concr. Compos.* **36**, 25–32 (2013). https://doi.org/10.1016/j.cemconcomp.2012.10.009

13. Konsta-Gdoutos M. S., Aza Ch. A. Self-sensing carbon nanotube (CNT) and nanofiber (CNF) cementitious composites for real time damage assessment in smart structures. *Cem. Concr. Compos.* **53**, 162–169 (2014). https://doi.org/10.1016/j.cemconcomp.2014.07.003

14. Hillerborg A. Analysis of fracture by means of the fictitious crack model, particularly for fiber reinforced concrete. *Int. J. Cem. Comps.* **2**, 177–185 (1980).

15. Hillerborg A. The theoretical basis of method to determine the fracture energy Gf of concrete. *Materials and Structures* **18**, 291–296 (1985). https://doi.org/10.1007/BF02472919

16. Carpinteri A., Ingraffea R. (eds). *Fracture Mechanics of Concrete: Material Characterization and Testing.* Hague, Boston, Lancaster, Martinus Nijhoff Publishers (1984).

17. Shah S. P. (ed.). *Application of Fracture Mechanics to Cementitious Composites.* Dordrecht, Boston, Lancaster, Martinus Nijhoff Publishers (1985).

18. Wittmann F. H. (ed.). *Fracture Toughness and Fracture Energy of Concrete.* Amsterdam, Elsevier (1986).

19. Elfgren L., Shah S. P. (eds). *Analysis of Concrete Structures by Fracture Mechanics.* London, New York, Tokyo, Melbourne, Madras, Chapman and Hall (1991).

20. Bazant Z. P. (ed.). *Current Trends in Concrete Fracture Research.* Dordrecht, Boston, London, Kluwer Academic Publishers (1991).

21. Shah S. P., Carpinteri (eds). *Fracture Mechanics Test Methods for Concrete.* London, New York, Tokyo, Melbourne, Madras, Chapman and Hall (1991).

22. Bazant Z. P. (ed.). *Fracture Mechanics of Concrete Structures.* London, New York, Elsevier Applied Science (1992).

23. Shah S. P., Swartz S. E., Ouyang C. *Fracture Mechanics of Concrete: Applications of Fracture Mechanics to Concrete, Rock and Other Quasi-Brittle Materials.* Wiley (1995).

24. Cotterell B., Mai Y. W. *Fracture Mechanics of Cementitious Materials.* London, Glasgow, Weinheim, New York, Tokyo, Melbourne, Madras, Blackie Academic & Professional (1996).

25. Bazant Z. P., Planas J. *Fracture and Size Effect in Concrete and Other Quasibrittle Materials.* CRC Press (1998).

26. Vipulanandan C., Gerstle W. H. (eds). *Fracture Mechanics for Concrete Materials: Testing and Applications.* American Concrete Institute (2001).

27. Gdoutos E. E. *Fracture Mechanics.* 3rd ed. Springer (2020).

28. Reda T. M. M., Xiao X., Yi J., Shrive N. G. Evaluation of flexural fracture toughness for quasi-brittle structural materials using a simple test method. *Can. J. Civ. Eng.* **29**, 567–575 (2002). https://doi.org/10.1139/l02-044

29. Karihaloo B. L., Nallathambi P. An improved effective crack model for the determination of fracture toughness in concrete. *Cement and Concrete Research* **19**, 603–610 (1989). https://doi.org/10.1016/0008-8846(89)90012-4

30. Moukwa M., Lewis B. G., Shah S. P., Quyang C. Effects of clays on fracture properties of cement-based materials. *Cement and Concrete Research* **23**, 711–723 (1993). https://doi.org/10.1016/0008-8846(93)90022-2

31. Das S. A. M., Dey V., Kachal R., Mobasher B., Sant G., Neithalath N. The fracture response of blended formulations containing limestone powder: Evaluations using two-parameter fracture model and digital image correlation. *Cem. Concr. Comp.* **53**, 316–326 (2014). https://doi.org/10.1016/j.cemconcomp.2014.07.018

32. Sarker P. K., Haque R., Ramgolam K. V. Fracture behaviour of heat cured fly ash based geopolymer concrete. *Mat. Design.* **44**, 580–586 (2013). https://doi.org/10.1016/j.matdes.2012.08.005

33. Nikbin I. M., Beygi M. H. A., Kazemi M. T., Amiri J. V., Rahmani E., Rabbanifar S., Eslami M. Effect of coarse aggregate volume on fracture behavior of self compacting concrete. *Const. Build. Mat.* **52**, 137–145 (2014). https://doi.org/10.1016/j.conbuildmat.2013.11.041

34. Stynoski P., Mondal P., Marsh C. Effects of silica additives on fracture properties of carbon nanotube and carbon fiber reinforced Portland cement mortar. *Cem. Concr. Comp.* **55**, 232–240 (2015). https://doi.org/10.1016/j.cemconcomp.2014.08.005

Received: February 12, 2022
Revised: March 1, 2022
Accepted: March 3, 2022

Authors' information:

Emmanuel Gdoutos — PhD, Academician, Prof.; egdoutos@civil.duth.gr
Maria Konsta-Gdoutos — Dr Sci., Prof.; maria.konsta@uta.edu

Механика разрушения полученных по растворной технологии нанокомпозитов, армированных углеродными нанотрубками

Э. Гдутос[1], *М. Конста-Гдутос*[2]

[1] Афинская академия наук, Греция, 106 79, Афины, ул. Панепистимиу, 28
[2] Техасский университет в Арлингтоне,
Соединенные Штаты Америки, 76019, Арлингтон, Техас, С. Неддерман Драйв, 701

Для цитирования: *Gdoutos E., Konsta-Gdoutos M.* Fracture mechanics characterization of mortar nanocomposites reinforced with carbon nanotubes // Вестник Санкт-Петербургского университета. Математика. Механика. Астрономия. 2022. Т. 9 (67). Вып. 3. С. 452–463. https://doi.org/10.21638/spbu01.2022.306

Целью данной статьи является исследование характеристик механики разрушения нанокомпозитов, изготовленных по растворной технологии, армированных многостенными углеродными нанотрубками (MWCNTs). Коэффициент интенсивности критического напряжения K_{Ic}, скорость выделения энергии деформации GI_c, эффективная длина трещины a_c и смещение раскрытия вершины трещины $CTOD_c$ определяются с использованием образцов с трехточечным изгибом. Было установлено, что армирование раствора MWCNTs обеспечивает существенное улучшение вышеуказанных характеристик механики разрушения.

Ключевые слова: механика разрушения, многостенные углеродные нанотрубки, коэффициент интенсивности напряжений, скорость выделения энергии, смещение вершины трещины, нанокомпозиты строительных растворов, цементирующие материалы.

Статья поступила в редакцию 12 февраля 2022 г.;
доработана 1 марта 2022 г.;
рекомендована к печати 3 марта 2022 г.

Контактная информация:

Гдутос Эммануэль — egdoutos@civil.duth.gr
Конста-Гдутос Мария — maria.konsta@uta.edu